HHS Public Access

Author manuscript

Nat Biotechnol. Author manuscript; available in PMC 2018 June 15.

Published in final edited form as:

Nat Biotechnol. 2017 November ; 35(11): 1087–1093. doi:10.1038/nbt.3978.

Programmable assembly of pressure sensors using pattern-forming bacteria

Yangxiaolu Cao[1], **Yaying Feng**[2,+], **Marc D. Ryser**[3,4,+], **Kui Zhu**[1], **Gregory Herschlag**[1,3], **Changyong Cao**[2,5], **Katherine Marusak**[2], **Stefan Zauscher**[1,2,6], and **Lingchong You**[1,7,8,*]

[1]Department of Biomedical Engineering, Duke University

[2]Department of Mechanical Engineering and Materials Science, Duke University

[3]Department of Mathematics, Duke University

[4]Department of Surgery, Division of Advanced Oncologic and GI Surgery, Duke University Schoolof Medicine

[5]School of Packaging, Department of Mechanical Engineering, Michigan State University, EastLansing, MI 48824

[6]Department of Chemistry, Duke University

[7]Center for Genomic and Computational Biology, Duke University

[8]Department of Molecular Genetics and Microbiology, Duke University School of Medicine

Abstract

Biological systems can generate microstructured materials that combine organic and inorganic components and possess diverse physical and chemical properties. However, these natural processes in materials fabrication are not readily programmable. Here, we use a synthetic-biology approach to mimic such natural processes to assemble patterned materials.. We demonstrate programmable fabrication of three-dimensional (3D) materials by printing engineered self-patterning bacteria on permeable membranes that serve as a structural scaffold. Application of gold nanoparticles to the colonies creates hybrid organic-inorganic dome structures. The dynamics of the dome structures' response to pressure is determined by their geometry (colony size, dome height and pattern), which is easily modified by varying the properties of the membrane (e.g., pore size and hydrophobicity). We generate resettable pressure sensors that process signals in response to varying pressure intensity and duration.

*Corresponding author. Department of Biomedical Engineering, Duke University, CIEMAS 2355, 101 Science Drive, Box 3382, Durham, NC 27708, USA., Tel.: +1 (919)660-8408; Fax: +1 (919)668-0795; you@duke.edu.
+These authors contributed equally to this work

Author contributions: LY and YC conceived the project. YC generated and analyzed all the experimental data. YC developed MATLAB codes for image analysis. YC and YF designed and carried out the electrochemical pressure sensing experiments. MDR and GH developed the numerical simulator for 3D pattern formation. YC conducted parameter fittings in all simulations and generated the final simulation results. CC developed the finite element simulations for strain analysis. KZ assisted with immunolabeling and TEM imaging. KM assisted with TEM imaging. YC, SZ, and LY wrote the manuscript, with inputs from YF, MDR, KZ, GH, and KM.

Conflict of interest statement: The authors declare no competing financial interests.

Nature presents many forms of microstructured materials, fabricated from the bottom up, that combine living and non-living components and have advantageous physical properties. For example, mollusk shells, composed of multilayered microstructures consisting of calcium carbonate interlaced with a small amount of organic components[1], are three orders of magnitude tougher than non-biogenic calcium carbonate[2,3]. In contrast to conventional physical and chemical synthesis methods, biological fabrication is environmentally friendly and often relies on the self-assembly of building blocks. Advances in synthetic biology and biomaterials engineering[4-6] have demonstrated the self-assembly of structures from various biological building blocks[7–10], including proteins[7-9], peptides[10-12], and DNAs[13-16]. Some of these structures combine organic and inorganic components. For example, the naturally occurring S-layer protein can self-assemble into different shapes such as sheets or open cylinders[17] and can serve as a template for assembling cadmium sulfide (CdS) nanocrystals into a superlattice structure[18-20].

Another form of hybrid organic-inorganic material uses engineering of bacteria to control the formation of biofilms that assemble inorganic compounds across various length scales. In a recent study, Chen *et al.*[21] use engineered bacteria to produce curli amyloid. The production and patterning of curli can be controlled by the timing and duration of the gene circuit inducer. The conductive biofilms generated from this inorganic-organic system combined with an electrode could be externally controlled as electronic switches[21]. However, the assembly of nanoparticles is mediated by pre-patterning of bacteria on a 2D surface combined with exogenous induction of curli expression. This approach limits the tunability of the physical properties of the assembled materials.

Here, we address these limitations by assembling nanoparticles through programmed self-organized pattern formation in engineered bacteria. We achieve this by further engineering an existing synthetic gene circuit that could program bacterial pattern formation[22]. The circuit consists of a mutant T7 RNA polymerase (T7RNAP)[23] that activates its own expression through a T7 promoter carrying an operator site (*lacO*) repressed by LacI, as well as that of LuxR and LuxI. LuxI synthesizes an acyl-homoserine lactone (AHL), a membrane-diffusible chemical that upon binding and activating LuxR, can induce expression of T7 lysozyme, which inhibits T7RNAP[24]. CFP and mCherry fluorescent proteins are co-expressed with T7RNAP and lysozyme, respectively, to report the circuit dynamics. When turned ON by addition of exogenous Isopropyl-D-1-thiogalactopyranoside (IPTG), the circuit enables generation of robust spatial patterns in the expression of mCherry[22,25].

We extended our 2-D patterning circuit[22] by incorporating an engineered curli developed by Chen *et al.*[21]. These bacteria are engineered to produce and assemble extracellular curli fibrils with functional tags into three-dimensional (3D) patterns. These patterned curli fibrils in turn enable assembly of inorganic materials. This two-layer control enables assembly of structured materials that have well-defined physical and chemical properties (Fig. 1), in our case, the capability to sense external pressure.

Fabrication of structured materials based on the programmed self-organization of living cells represents the next frontier at the interface of synthetic biology and materials engineering. It

draws inspiration from biological fabrication in nature; yet it applies engineering principles to achieve predictable control of material structures and functions at two layers: programmed self-organization of cells and assembly of cellular products to interact with the environment. A pressure sensor assembled by living cells offers many other possibilities for future material fabrication, which includes dynamical restructuring in response to environmental cues, integration of mechanical signals and chemical signals, and self-healing of the functional structures.

Curli is part of the extracellular matrix produced by many bacteria and consists of two components, CsgA and CsgB[26]. Chen *et al.*[21] engineered CsgA to encode six histidine tags (6×-His tag) to interface with inorganic materials. We modified our circuit to co-express the engineered CsgA with the lysozyme, generating the curli-pattern circuit. We then used *E. coli* MG1655 *PRO ΔcgA ompR234*, in which csgA is deleted but *csgB* is constitutively expressed, as a host strain for our engineered CsgA-His (hereafter referred to as MG1655 *ΔcsgA*).

MG1655 *ΔcsgA* cells without a gene circuit generated no detectable curli fibrils (Supplementary Fig. 1A). When induced by IPTG and AHL, however, MG1655 Δ*csgA* cell carrying the curli-pattern circuit led to curli formation (Supplementary Fig. 1b, c) in a dose-dependent manner (Supplementary Fig. 1d). Addition of exogenous AHL allows activation of curli without requiring a high culture density.

These curli fibrils enabled assembly of gold nanoparticles conjugated with a Ni-Nitrilotriacetic acid (NTA) group, through the formation of a Ni (II)-NTA bound between the 6×-His tag and the gold nanoparticle (Supplementary Fig. 1E). To assemble other inorganic particles, we used a mouse anti-6× His tag antibody conjugated biotin, which can bind to anti-mouse antibody conjugated with nanoparticles. As a demonstration, we used goat anti-mouse IgG conjugated with 10 nm gold. Assembly of the gold particles occurred when both antibodies were present (Supplementary Fig. 1f), but not when either was absent (Supplementary Fig. 1g). By changing the conjugation module on the secondary antibody we can assemble different inorganic nanoparticles, including CdSe quantum dots (Supplementary Fig. 1h).

Generation of tunable bacterial patterns in 3D

We used inkjet printing[25] to initiate single colonies on permeable membranes placed on top of agar containing growth media. The membranes serve as a structural support for colony growth and greatly facilitate subsequent assembly of nanoparticles. Briefly, we printed a 150 pL (containing ~20 cells) droplet of the bacterial culture onto each membrane. When confined in 2D, bacteria carrying our pattern formation circuit generated 2D patterns[25]. Here we did not confine the bacterial growth to enable 3D pattern formation. After a 32 hr incubation at 30°C, each colony grew into a raised, convex shape, with a 3D dome pattern of mCherry expression within (Fig. 2a and Supplementary Fig. 2a). The colony size, elevation, and the corresponding pattern were controllable by the hydrophobicity and pore size of the membrane. For a fixed pore size, the colonies became flatter with decreasing membrane hydrophobicity. If a membrane was too hydrophobic (e.g., a PTFE membrane), it prevented

colony growth, likely by suppressing wicking of nutrient from the agar and making it unavailable to the bacteria[27]. For membranes of the same material (thus with similar hydrophobicity), the colonies became larger but not taller with increasing pore sizes (Fig. 2b and Supplementary Fig. 2b).

Mechanistically, the observed dependence of colony shape on the physical properties of the membrane can be attributed to modulation of cellular motility on, and nutrient transport across the membrane. We developed a phenomenological kinetic model that accounts for these effects to examine how colony morphology and gene expression patterns are controlled by the physical properties of the membranes. Indeed, the model captured the characteristics of the dome structure, as well as its dependence on membrane properties (Fig. 2c and Supplementary Fig. 2c). Similarly, consistent with experimental observations (Fig. 2d and Supplementary Fig. 2d), our model shows that decreasing hydrophobicity leads to colonies with larger radii and smaller heights (Fig. 2e and Supplementary Fig. 2e).

Assembly and evaluation of pressure sensors

We next assembled gold nanoparticles using the bacteria carrying the curli-pattern circuit. Briefly, we fixed each colony by floating the supporting membrane on high concentration fixation solution and then immunolabeled gold nanoparticles onto the structure (Supplementary Fig. 3a and Supplementary Text). As curli and mCherry are co-expressed, we expect their spatial patterns to overlap. Therefore, the structure of gold nanoparticles assembled by curli should also overlap with that of mCherry. Indeed, confocal microscopy shows that the spatial distribution of the nanoparticles is similar to that of mCherry (Supplementary Fig. 3b), both forming a dome.

The dome is a composite material consisting of inorganic gold nanoparticles distributed in an organic matrix. As the organic matrix is visco-elastic[28,29], and the gold nanoparticles are conductive, we conjectured that the assembled microstructure could serve as a pressure sensor. Consider two bacterially fabricated domes facing each other and separated by a small distance, and a constant voltage applied to the edge of each dome (Supplementary Fig. 4a). When sufficiently pressed, the two domes make contact, which leads to the flow of an electrical current. Since the inter-particle distances decrease and the number of particle-particle contacts increase, the strength of the current should reflect the strength of the externally applied pressure.

To test this notion, we used nitrocellulose to mount a nuclepore track-etched polycarbonate (PC) membrane with a colony onto a thin glass coverslip. We then positioned two such glass coverslips (each carrying a colony) to face each other with a 0.5 mm thick silicone gasket as a spacer in between (Supplementary Fig. 4b). Next, we used copper wire to connect the edges of the colonies to an electrochemistry workstation. The workstation provided a constant voltage to the device and recorded the changes in the electronic current flowing through the device. To actuate this pressure sensitive device, we placed a thin cylinder (~1.5 mm in diameter) right on top of the upper glass coverslip. The center axis of the cylinder was aligned with the center of the two colonies. The device was then actuated by a programmable syringe pump, pressing on the cylinder (Supplementary Fig. 4c).

The displacement of the actuator had different profiles, depending on how fast and how strong two colonies were pressed together or separated (Fig. 3 a and b). We first tested the pressure response of colonies not containing the programmed structures. We used MG1655 *ΔcsgA* cells expressing the histidine-tagged CsgA under the induction of AHL[21]. When curli expression was fully induced, the assembled gold nanoparticles were distributed approximately uniformly in the colonies, forming a solid spherical cap (Supplementary Fig. 3c, third column). We controlled the radii and heights of different colonies by using membranes with different pore sizes, where a larger pore size generates colonies with larger radii and height. Because each colony's height was >250 μm, the two opposing colonies were already in contact even without applied pressure (Fig. 3c, orange line), leading to a high base-level current. Although the current increased when the two colonies were pressed together, it did not significantly vary with different displacement profiles (Fig. 3c, magenta line). The lack of a strong differential response is more evident by plotting the current response against the displacement distance. Increasing displacement (i.e., increasing pressure on the device) did not cause a significant difference between the overall current levels (Fig. 3d, left and middle panels). A control experiment showed that the gold nanoparticles assembled in curli were critical for making the colonies conductive, as pressing together two colonies containing no gold nanoparticles generated no detectable current (Fig. 3c, black lines; Fig. 3d, right panel).

In contrast, the domes containing gold nanoparticles exhibited differential pressure responses. To control the dome shape, we grew the bacteria carrying the curli-pattern circuit on PC membranes with different pore sizes, before incubating with gold nanoparticles. The resulting colonies had different radii but approximately the same height (Supplementary Fig. 2b). The height was sufficiently small such that two colonies placed opposite each other in our device were not in contact without being pressed. Thus, in the off-state (without externally applied pressure) the electrical current through the device was near zero. When the two colonies were pressed into contact, the resulting current increased with increasing applied pressure (Fig. 3e). For the colonies without a dome structure, the maximal responses to the first two presses were similar (Fig. 3c), even though the second press was stronger than the first. That is, these colonies did not exhibit differential pressure responses. In contrast, for the colonies with dome structure, the maximal response to the second press was twice as large as that to the first press, demonstrating differential pressure response (Fig. 3e). We speculate that with increasing pressure, the deformation of the dome structure would cause tighter packing of nanoparticles near the contact point. This in turn would increase the number of conducting pathways through the device, and as a consequence, an increased electrical current (Fig. 3e, red arrows).

We also found that a device with smaller domes (i.e., those with smaller radii of curvature) exhibited a stronger pressure response than one containing larger domes (Fig. 3e). This response is likely due to two reasons: first, different domes would have similar electrical resistivity because the densities of gold particles would be similar among all domes. Thus, a smaller dome would have a smaller resistance than a larger dome. Second, given the same pressing distance, the strain is higher in a smaller dome compared with that in a larger dome at the same relative location within the colony. Therefore, there will be more particle-particle contact in smaller domes, which in turn would increase the conductivity. These

interpretations are consistent with the results from finite element simulations of strain and pressure experience by two domes when pressed (Supplementary Fig. 5). Because these domes were elastic, the device could be pressed multiple times and show a resettable and robust readout (Fig. 3e and Supplementary Fig. 6, 7). When the pressing distance increased, there was a dramatic increase in current flowing through a device with two small domes (Fig. 3f,). The differential pressure response was smaller for a device with two larger domes (Fig. 3f,).

In contrast to solid spherical cap structures, the dome-shaped structures had strong differential responses to pressure (Fig. 3C, E). In a solid spherical cap structure with gold nanoparticles uniformly distributed, there are more conducting pathways for electrons (Fig. 3C, red arrows) than in a dome structure (Fig. 3E, red arrows). Thus, a change in the pressing distance between two colonies would have little effect on colony resistance. Given the same change in the pressing distance, the number of conductive pathways will increase more dramatically with an increasing contact area in a dome structure.

Due to the viscoelastic behavior of the bacterial colonies, the distribution of gold nanoparticles embedded in the domes would likely respond with different conduction dynamics to different pressing profiles (Fig. 4A). Without pressure, the distribution of gold nanoparticles in each dome is similar (time point 1). When two domes are pressed together (time point 2), the contact region of the two opposing domes increases and the exerted pressure leads to a densification of the local distribution of gold nanoparticles. If the displacement of the actuator is maintained, i.e., the strain on the device is held constant (the flat region between points 2 and 3, Fig. 4A), then the density of the gold nanoparticles in the contact region should decrease as the stress in the visco-elastic matrix relaxes (Fig. 4B), and should lead to a concomitant decrease in conductivity. In other words, at constant strain we expect to see the current flow through the device to drop. Our experimental observations confirmed this prediction. Note in Fig. 4C, the reduced response corresponding to the plateau between time points 2 and 3 in the input.

The bacterially assembled domes are robust pressure sensors – even without the precision of control by using a syringe pump. As an illustration, we used a pressure sensor consisting of two facing colonies to control an LED light (Fig. 5A). This device exhibited robust responses to manual pressure using a finger. When pressed with increasing strength, the conductivity of the pressure sensor increased and led, after amplification, to an increasing LED brightness. The brightness gradually decreased when the pressure was removed. The pressure sensor responded similarly when it was repeatedly pressed (Supplementary Video 1).

Signal processing using bacterially assembled pressure sensors

The ability of the sensors to transduce differential pressure inputs makes it possible to construct more complex signal processing devices. Given the same sequence of input pressure signals with alternating strengths (Fig. 5B, left panel), domes of different size would yield different responses that could be integrated by a downstream signal processor. As a demonstration, we used domes of different radii but similar heights (as controlled by

membrane pore size). Each would generate its characteristic response to an alternating sequence of strong and weak pressure signals (Fig. 5B, i and ii). We then used a current-canceling circuit to subtract one response from the other. The net response exhibited distinct peaks corresponding only to strong input signals, but not to small ones. That is, the integration of these two responses led to a filtering of small variations in the pressure input (Fig. 5B, iii and iv). The readout shown in Fig. 5B-iii is not the exact subtraction of those resulting from individual sub-circuits (Fig. 5B, i and ii), in part due to the noise arising from the bacterial assembly of nanoparticles, assembly of the subtraction device, and manual operation of the device. Conversely, we used a current-adding circuit to integrate the two intermediate responses, and the overall response exhibited distinctly amplified peaks corresponding to original inputs (Fig. 5B, i and ii). Similarly to the subtraction device, the readout of the addition circuit (Fig. 5B-iii) does not correspond to the exact addition of the signals from individual sub-circuits (Fig. 5B, i and ii).

By placing multiple domes in appropriate spatial configurations in electronic circuits, we were able to implement location sensors (Supplementary Fig. 8). Each location sensor is activated when a dome is pressed and the overall resistance of the sensor is determined by the location of the pressed dome. The amplitude of the output (electric current) thus reflects the location of the pressed dome. To illustrate this design concept, we implemented multiple location sensors consisting of two, three, or four pairs of bacterially assembled gold-nanoparticle domes. Each location sensor functioned as designed (Supplementary Fig. 8).

Finally, by combining with other electronic components, we implemented a bacterial “touch-pad” depicted in Fig. 1C (Supplementary Fig. 9A). Different from the locational sensor shown in Supplementary Fig. 8, this touch-pad enabled generation of diverse output signals. Pressing on a bacterial sensor site in the “touch-pad” triggered activation of LED at the location (Supplementary Fig. 9B). Pressing on a location that deformed multiple sensors, would trigger activation of multiple LEDs (Supplementary Fig. 9C). This system demonstrates the capability of utilizing bacterially assembled materials as building blocks for fabricating functional devices.

Discussion

Progress in programming spatial patterns in cell populations[25,30-34] has lagged behind other developments in synthetic biology, such as programming of logic functions[5,35-39], temporal dynamics of single cells[40,41], or temporal dynamics of cell populations[42-44]. The scarcity of successful pattern-forming circuits is due to the intrinsic challenges associated with both modeling and experiments[45]. In particular, modeling spatiotemporal dynamics is typically more time-consuming and less intuitive than modeling only temporal dynamics. Similarly, experimental demonstration of patterning dynamics is typically much more difficult than that of temporal dynamics alone. Our results demonstrate programming of 3D materials from a self-patterning colony by coupling gene circuit dynamics with modulation of environmental conditions. In contrast to previous efforts to assemble materials using engineered bacteria[21,46], our work is based on the principle of programmed self-organization. Each bacterium carrying the circuit contains all the information to grow into the final structure (dome), without pre-patterning. The pressure-sensing capability that we

demonstrate emerges from this engineered structure; it would have been difficult to achieve by direct assembly of gold nanoparticles by pre-patterning of curli expression[21].

In addition to pressure sensors, such biologically fabricated structured materials could have other applications, such as in plasmonics. For instance, if the domes containing gold could be used as a back contact with solar cells while coated with a dielectric material, the system could be applied to couple or trap sunlight for improved photon absorption in photovoltaics[47,48].

In future development of our approach, engineered curli could be used to assemble other inorganic materials to expand the functionality of the dome structure. For example, replacement of the gold nanoparticles with catalytic metal nanoparticles (i.e., CoP) could produce dome structures coated with catalytic sites for applications in water splitting[49]. Diverse tunable patterns could also be generated by varying the gene circuit and the growth conditions. Here we achieved tunability (varying height or width of the colony) primarily by controlling membrane properties. However, pattern formation can be further tuned by adjusting circuit parameters, such as the strength of positive feedback, the burden of circuit activation, or the strength of cell-cell communication[22,25]. Alternative circuits can generate other patterns[31,32,34] by one or multiple engineered populations, and the engineered curli can be replaced by other effector molecules to assemble soft materials, such as self-organized hydrogel formation[50]. Other organisms, such as yeast, could allow further variations in pattern formation[51]. Engineering at multiple time and length scales could enable the predictable 3D assembly of materials for diverse applications in medicine[52,53], biotechnology[54,55] and environmental cleanup[56,57]. The ability to generate programmable 3D patterns may also facilitate the study of the design principles of natural 3D patterning processes, such as skeletal patterns in limb[58], tooth[59,60], and biofilms[61,62].

Online Methods

Plasmids, cell strains, and growth media

The curli-pattern circuit consists of two plasmids: pET15bLCFPT7 and pTuLysCsgA$_{His}$2CMR2, as described in the supplementary material. As a control, we used pZA-CmR-rr12y-pLuxR-*csgA*$_{His}$[21] for induced expression of curli protein. Unless noted otherwise, MG1655 *PRO* Δ*csgA ompR234* cells carrying the curli-pattern circuit or the control plasmid was used for the printing experiments. For initial overnight culture, LB medium was used; for liquid culture experiments, M63 minimum medium supplemented with 0.2% w/v glucose and 1mM $MgSO_4$ was used; for growth on membrane experiments, 2×YT medium was used[63]. All media were adjusted with 1.0M KOH (Sigma) solution to PH=6.5 by VWR Symphony SB70P PH meter.

Measurement of cell density in liquid culture

Cell densities of liquid cultures were quantified using optical density (OD) measured at 600 nm absorbance using a Perkin-Elmer VICTOR3 plate reader.

Transmission electron microcopy (TEM)

10 μl fixed sample was deposited onto a 200-mesh formvar/carbon coated nickel TEM grid (Electron Microscopy Sciences) for 2 mins, then stained with 2% uranyl acetate (Electron Microscopy Sciences) for 30s. TEM images were obtained on FEI Tecnai G² Twin transmission electron microscope at 80 kV accelerating voltage. All these parameters were kept the same between experiments.

Scanning electron microscopy (SEM)

1 cm × 1 cm silicon wafer was immersed in 1 ml sample solution overnight. After fixation and dehydration process, wafer with samples were imaged under FEI XL30 SEM-FEG scanning electron microscope with 10kV accelerating voltage. Images were obtained at ultra-high resolution, using the secondary electron imaging mode. All these parameters were kept the same between experiments.

Confocal microscopy

Samples were imaged with a Zeiss 780 confocal upright fixed stage confocal microscope using a 10×/0.45 Dry Zeiss Plan-Apochromat 1063-139 WD 2.0 mm objective. For mCherry observation, the samples were excited at a 561 nm, the emission was detected through 576 nm and 696 nm bandpass filters. All these imaging parameters were kept the same between experiments.

Electrochemical measurement

Currents though the device were measured with a Bio Logic SP-200 electrochemistry workstation, at 1 V applied voltage.

Inkjet printing[25]

We used the Epson Stylus Photo R280 Ultra Hi-Definition Photo Printer (C11C691201) for printing experiments for three reasons [64]. First, this printer contains a CD tray, which provides the capability of printing on a solid flat surface. After the culture well was loaded on the CD tray, the printing template could be designed to match the corresponding position of the culture well. Second, the inkjet is piezo-activated, which will not affect the cell viability. Third, the printer has a high resolution: 5760×1440 pixels at the maximal dots per inch (dpi), which enables precise control of initial seeding positions of bacteria.

To facilitate the manipulation and sterilization, the outer shell of the printer was disassembled and removed. We then used PrintPayLess six packs Empty Refillable Ink Cartridges instead of the original ink cartridges.

Print heads were cleaned thoroughly before and after each experiment. First, the printer head box was repositioned to the middle of the printer trail and absorbent paper towels were placed under the printer head to collect the liquid flushing through the printer heads. Second, the printer heads were flushed with 75% ethanol once, followed with washing with deionized water three times gently using a syringe. The absorbent paper towels were removed and the printer head box was then placed back in its original spot.

To prepare 0.3% agar for printing, we mixed 0.15 g of agar (214530 Difco™ Agar, Granulated) in 50 ml of 2×YT medium, and microwaved the mixture until it was homogenous with no aggregates. We then cooled the agar below 50°C at room temperature, and supplemented it with 50 μg/mL kanamycin, 50 μg/mL spectramycin, 75 μg/mL carbenicillin, 50 μg/mL chloramphenicol, and 1000 μM β-D-1-thiogalactopyranoside (IPTG) and 100nM acyl-homoserine lactone (AHL). We next pipetted 170 μL of the agar into each culture well, and let it solidify at room temperature.

An overnight culture of MG1655 *ΔcsgA* cells carrying the full circuit was diluted to 0.2 absorbance (measured by Victor 3 plate reader) and then diluted another 50-fold into fresh LB broth. The diluted culture was transferred into a tone empty ink cartridge using a sterile syringe. The other five cartridges were filled with deionized water sterilized using a 0.2 μm filter (VWR® Syringe Filters, # 28145-477).

Before printing, a porous membrane (Whatman, plc) was placed on top of the solidified agar. Printing templates were designed in software GIMP using 1-pixle diameter spot. Each template was exported to an Epson CD printer program to direct printing of bacteria onto the membrane surface. After printing, the whole device was incubated under 30 °C for 32 hrs.

NiNTA-AuNP labelling

The protocol is adapted from[21]:

1. 20 μL of bacterial culture was placed on parafilm with TEM grid floating on top. The coated side of the TEM grid was in contact with the culture for 2 mins.
2. The TEM was washed by 20 μL of 1× phosphate-buffered saline (PBS) 5 times (1 min for each time).
3. The TEM grid was placed on top of 20 μL of selective binding buffer (1× PBS with 0.487 M NaCl, 80 mM imidazole, and 0.2% Tween20) for 3 times (1 min for each time).
4. The TEM grid was placed on top of 50 μL of selective binding buffer with 10 nM 5 nm NiNA-AuNP particles (Nanoprobes) for 90 mins.
5. The TEM grid was washed 5 times (1 min for each time) with 20 μL of selective binding buffer, and 3 times (1 min for each time) with 20 μL of 1× PBS.
6. Before imaging under TEM, the grid was stained with filtered 2% uranyl acetate for 30 s.

Immunolabeling nanoparticles to the colonies (Supplementary Fig. 3A)

1. After peeling the membrane from the agar, a membrane was washed twice by floating on top of 1 × PBS twice, each wash lasted for 5 mins.
2. The membrane was placed to float on top of 8% formal aldehyde for 24 hrs to fix the colony. After the fixation, membrane was taken out and air-dried for 5 mins.
3. The membrane was washed with PBS twice by floating on top of 1× PBS, each wash lasted for 5 mins.

4. After wash, membrane was placed on top of blocking buffer (6% BSA (RIA grade, Sigma Cat. no. A-7888) in 1× PBS) for 1 hr at room temperature.

5. The membrane was incubated in the primary antibody (mouse anti-6× His tag antibody conjugated with biotin, Thermo Fisher Scientific, # MA1-21315-BTIN) diluted 1000 fold in blocking buffer overnight at 4 °C.

6. Followed with three times 1× PBS wash (5 mins for each wash), the membrane was incubated in the secondary antibody (goat anti-Mouse IgG conjugated with 10nm gold particles, Life Science Technologies, LLC, # G7652) diluted 10 fold in blocking buffer for 2 hrs under room temperature (note: secondary antibody in Supplementary Fig. 1H is Streptavidin-655Qdots, Life Science Technologies, LLC, # Q10121MP).

7. The membrane was washed in 1× PBS three times (5 mins for each wash).

In our experiments, gold nanoparticles were added to saturation, such that the resulting structures will be determined by the engineered dome patterns (as illustrated in Supplementary Figure 3B). In particular, we chose the concentration such that: 1) the concentration is high enough to saturate the gold particles binding reaction; 2) the concentration cannot be not too high to cause self-aggregation of the gold nanoparticles. In particular, when the concentration was too high, we observed self-aggregation of gold nanoparticles. After multiple tests, we found that 10-fold dilution of the original gold nanoparticle conjugates to be the optimal dilution.

Finite element simulations (Supplementary Fig. 5)

To provide insights into how domes with different radii responded differently to the same pressing, we performed finite element simulations for the compression process. All these simulations were carried out using the commercial finite element package ABAQUS (SIMULIA, Providence, RI). The height of all dome structures is 200 μm. The radii of small and large domes are 300 and 420 μm, respectively. The thickness of the mixture layer (t) from cell and gold nanoparticles is assumed to be 1/5 of the dome height (Supplementary Fig. 5A, left). Based on the mechanical properties of biofilm and polymers reported in literature[29], we modeled the elastic colony dome as an incompressible neo-Hookean material with Young's modulus of E_1 = 100 MPa. The mixture layer of cells and gold nanoparticle with same model was assumed to a larger modulus of E_2 = 200 MPa. Eight-node linear brick, hybrid elements, with reduced integration (C3D8RH) were used for all the simulations and a mesh sensitivity study was carried out to ensure the accuracy of the results (Supplementary Fig. 5A, right). A total of 228,656 and 111,392 C3D8RH elements were respectively used for the larger and smaller domes. A perfect bonding between the two different layers was assumed. The bottom surface of the lower dome was completely fixed, and a displacement load of 50 μm was incrementally applied to the top surface of the upper dome. The contact model between two domes was assumed to be general smooth contacts without friction. Quasi-static non-linear simulations were performed using ABAQUS/Standard.

For the pressure sensor consisting of a pair of domes, the total electrical resistance includes two parts: one is the materials resistance from the two colonies with dome structures, the other is the contact resistance between the contacting interface of the colony domes, which is the dominated factor that affects the conductivity of the devices[65].

For rough surfaces with microscale and nanoscale structures, the electrical contact resistance between two conductors is controlled by contact pressure and interface smoothness[65-67]. Regardless of the interface smoothness, the resistance between the pair of domes should decrease with the contact pressure[65-67]. Our simulations show that the smaller dome demonstrates a larger (~14.5% more) average contact pressure at the contact surface area of the domes (Supplementary Fig. 5D), resulting in a smaller resistance and thus a larger current flow. Our simulations show that this conclusion is still maintained for a wide range of variations in the modulus ratio (E_2/E_1) of the materials (Supplementary Fig. 5E) and the mixed layer's thickness (Supplementary Fig. 5F).

When compressed at the same distance (50 μm), the smaller domes experience much higher strains than do the larger domes (Supplementary Fig. 5B, C). The average strain along the middle interface of the conducting mixture layer in the smaller domes is ~23.8% larger than that in the larger colony domes. Therefore, more particle-particle contacts can be expected in smaller domes, which would consequently reduce the resistance and in turn increase the total conductivity.

Model development

Colony growth dynamics—To better understand and predict the experimental outcomes, we develop a phenomenological model to describe colony growth and gene expression. In particular, by assuming the separation of time scales, we decouple the colony growth from the gene circuit dynamics by first modeling growth in the absence of the circuit and then considering the gene expression based on the final shape of the colony.

Because of its radial symmetry when growing on top of a flat membrane (Fig. 2A), we characterize the colony by two variables:

1. The radial extension $R(t)$ on the membrane at time t
2. The height function $h(r, t)$, which determines the height of the column of cells situated at a distance r from the center of the colony.

Colony growth is regulated by the amount of nutrient in the colony, $N_c(t)$, which in turn depends on the amount of nutrient in the agar, $N_a(t)$.

Our model consists of the following differential equations:

$$\begin{cases} \dot{R} = v\dfrac{n_c}{n_c + K_p} \\ \dot{h}(r,t) = \gamma\dfrac{n_c}{n_c + K_p}h(r,t)\dfrac{Q_m}{Q^m + h(r,t)^m},\ 0 \le r \le R \\ \dot{n}_a = -\alpha_1 R^2(n_a - n_c) \\ \dot{N}_c = \alpha_2 R^2(n_a - n_c) - \beta_m\dfrac{n_c}{n_c + K_m}V_c - \beta_p\dfrac{n_c}{n_c + K_p}V_p \end{cases} \quad (1)$$

where,

- $n_a(t) = \frac{N_a(t)}{V_a}$ is the nutrient concentration in the agar at time t and V_a is the volume of the agar;
- $V_c(t) = \int_{r<R(t)} h(r)dr$ is the volume of the colony at time t;
- $n_c(t) = \frac{N_c(t)}{V_c(t)}$ is the nutrient concentration in the colony at time t;
- $V_p = \int_{r<R} h(r)\frac{Q_m}{Q^m + h(r)^m}dr$ is the total volume of cells that undergo proliferation;
- other constants in Eq (1) are explained in Supplementary Table 1.

In deriving the above equations, we made the following assumptions:

1. The colony expands radially at a speed that depends on the nutrient concentration (n_c), analogous to Monod kinetics (see[25] for details). With saturating nutrients, the colony exhibits traveling wave solutions with an asymptotic speed v. Because cells consume nutrients, depletion of nutrient leads to decrease in the wave speed as modeled by means of the $\frac{n_c}{n_c + K_p}$.
2. At each position r where the colony touches the membrane ($0 \le r \le R$), the colony has avertical growth rate $h(r, t)$ that increases with the availability of nutrient ($\frac{n_c}{n_c + K_p}$) and decreases with the height ($\frac{Q_m}{Q^m + h(r,t)^m}$).
3. We assume fast diffusion of nutrient in both agar and colony, leading to a homogeneous distribution in each compartment. Nutrient transfer from agar to colony takes place across the membrane. The rate of exchange is proportional to the area of contact between colony and membrane and the concentration gradient between the two compartments. The nutrient exchange accounts for the third equation and the first term in the fourth equation in (1).

4. In the colony, nutrient is depleted by the cells. We assume all cells to have a baseline metabolic resorption rate, captured by the second term in the fourth equation in (1). The last term in the equation accounts for depletion by cells undergoing proliferation.

In the experiments, the membrane pore size ρ and hydrophobicity (as measured by the contact angle θ) were varied as control parameters. To account for the impact of these parameters on the model, we assume that the radius expansion rate (v) is a function of the pore size (ρ) and the membrane contact angle (θ), and that the fitting constant for nutrient loss by transport (α_1) is a function of ρ. More precisely, we use the following empirical equations:

$$v = \left(\frac{20}{(1 + \frac{\theta}{40})^{10}} + 0.1 \right) (v_1 \rho^2 + v_2), \quad (2)$$

where $v_1 = 0.25\ \mu m^{-1} hr^{-1}$, $v_2 = 0.95\ \mu m\ hr^{-1}$ and

$$\alpha_1 = v_3 \rho^2, \quad (3)$$

where $v_3 = 0.01 \mu m^{-4}$

The contact angle made by water droplets and the surface provides a measure of hydrophobicity of the surface. Because the bacterial colony is mostly made of water, this will also provide us with a sense of how attracted the colony is to the surface. Water droplet equilibration is driven by surface energy, meaning that the contact angle may be used to determine the final shape of the droplet. On the other hand, colony growth is driven by interior mechanical forces (surface tension is negligible), meaning that the contact angle cannot be used to determine the final shape of the colony. Most importantly, the surface interaction with the growing colony will affect the ratio between vertical and horizontal growth rates. The contact angle of the colony is an emerging, rather than driving factor in colony growth. Due to this observation along with the simplifications in our model, we do not expect the model to empirically recover the less important contact angle, but do expect the model to recover the more important ratio of colony height-to-width.

Before simulating the colony growth, we rescale the variables as

$$\widehat{n_c} = \frac{n_c}{K_p}, \ \widehat{n_a} = \frac{n_a}{K_p}, \ \hat{h} = \frac{h}{Q}, \ \hat{t} = t\gamma$$

The model equations can be rewritten using the parameter groups G_i (see Supplementary Table 2),

$$\begin{cases} \dot{R} = G_1 \dfrac{\widehat{n_c}}{\widehat{n_c}+1} \\ \dot{\hat{h}}(r,t) = \dfrac{\widehat{n_c}}{\widehat{n_c}+1}\hat{h}(r,t)\dfrac{1}{1+\hat{h}(r,t)^m} \\ \widehat{n_a} = -G_2R^2(\widehat{n_a}-\widehat{n_c}) \\ \dot{N}_c = G_3R^2(\widehat{n_a}-\widehat{n_c}) - G_4\dfrac{\widehat{n_c}}{\widehat{n_c}+G_5}V_c - G_6\dfrac{\widehat{n_c}}{\widehat{n_c}+1}V_p \end{cases} \quad (4)$$

Because systems (1) and (4) are infinite dimensional (the equation for h is defined for each $r < R$), we discretize the radial dimension of the colony into 100 equally spaced elements of size 50. We then solve the resulting system of ODE using a stiff differential equation solver (ode23s) in MATLAB. The initial conditions are specified as: $R(0) = 0.1$; $\hat{h}(r, 0) = 0.1(0 \le r \le R(0))$; $\widehat{n_a}(0) = 50$; $N_c(0) = 0$. The computational domain only provides the computational range for running the simulation. Consequently, we choose a computational domain large enough to avoid pattern interference with the boundary and to enforce no-flux boundary conditions.

Expression profiles

Based on the model of the colony growth dynamics developed in the previous section, we can now quantify the final gene expression profiles. To this end, we use the above model to compute the colony shape in the quasi-stationary state where nutrient has been depleted. We then compute the corresponding steady-state profiles of T7RNAP (denoted as T) and T7 lysozyme (denoted as L), the T7-lysozyme complex (denoted as P), and AHL (denoted as A). The equilibrium equations for gene expression are given by the following nonlinear system, see[25] or details and Supplementary Table 2,

$$\begin{cases} \dot{A} = 0 = -G_7\int_\Omega \dfrac{T}{1+T}\dfrac{1}{1+P}\varphi(r,K)dV - G_8A & (5) \\ \dot{L} = 0 = -G_9L + G_{10}\theta(C)\dfrac{T}{1+T}\dfrac{A^M}{1+A^M}\varphi(r,K) & (6) \\ \dot{T} = 0 = -G_{11}T + G_{12}\theta(C)\dfrac{T}{1+T}\dfrac{1}{1+P}\varphi(r,K) & (7) \\ P = \dfrac{G_{13}}{G_{14}G_{15}}TL & (8) \end{cases}$$

where the function φ represents the gene expression capacity,

$$\varphi(r,c) = \begin{cases} \dfrac{K^n}{K^n+(R-r)^n}, & r \le R \\ 1, & r > R \end{cases} \quad (9)$$

With R the colony radius, see (1) and (4). In (6) and (7), θ is the Heaviside function ($\theta(x) = 1$ if $x > 0$ and $\theta(x) = 0$ otherwise). C is the cell density, when cell density reach the carrying capacity, $C = 1$.

Ignoring A for a moment, the equations (6) - (8) form a cubic polynomial system in T and L. One can determine the solution of this system analytically and find that there is one zero root. The remaining roots are either complex, or one is positive definite and the other negative definite. We assume that the steady state will obtain the positive root if it exists, and the zero root otherwise. At this point, given a value for A, we can compute the steady state profile for T and L, however Eq (5) will not be satisfied. To find a simultaneous solution we performed the following iterative procedure:

1. Make an initial guess for $A = A(0)$.
2. Predict $L(0)$ and $T(0)$ based on $A(0)$ by solving equations (6) - (8).
3. Update the prediction for $A(0)$ by solving equation (5), to determine $A(1)$.
4. Repeat steps (2) and (3) until the solution has converged.

In practice, we found convergence after as few as three steps of the iterative procedure with the parameters listed in Supplementary Table 2. Finally, we note that the growth model is built on the assumption of an incompressible bacteria colony with a sharp interface. In reality, the proliferating colony front is less dense than the core – because of this difference, we expect to see differences in profiles near the colony boundary.

Statistical analysis

Statistical analyses were performed with MATLAB (R2015b). Data are presented as mean +/- standard deviation (s.d.) with sample numbers n noted in the figure legends. For detailed information, please also refer to “Life Sciences Reporting Summary”.

Data availability statement

The sequence data of plasmid pET15bLCFPT7 are available on Addgene, ID53545; the sequence data of plasmid pTuLys2CMR2 are available on Addgene, ID53544.

Supplementary Material

Refer to Web version on PubMed Central for supplementary material.

Acknowledgments

We thank R. Tsoi, C. Zhang, Z. Dai for discussions and comments; Y. Gao for assistance with confocal microscopy; Duke Light Microscopy Core Facility (LMCF) for access to confocal microscopes and imaging software; Michelle Plue for assistance with the TEM and SEM; Duke Shared Materials Instrumentation Facility (SMIF) for access to TEM and SEM. This study was partially supported by the Office of Naval Research (N00014-12-1-0631), National Science Foundation (L.Y.), Army Research Office (L.Y., #W911NF-14-1-0490), National Institutes of Health (L.Y.: 1R01-GM098642; M.D.R: R01-GM096190; K99CA207872-01), Swiss National Science Foundation (M.D.R: P300P2_154583), a David and Lucile Packard Fellowship (L.Y.).

References and notes

1. Currey JD. Mechanical-Properties of Mother of Pearl in Tension. Proc R Soc Ser B-Bio. 1977; 196:443–+. DOI: 10.1098/rspb.1977.0050
2. Luz GM, Mano JF. Mineralized structures in nature: Examples and inspirations for the design of new composite materials and biomaterials. Compos Sci Technol. 2010; 70:1777–1788. DOI: 10.1016/j.compscitech.2010.05.013
3. Jackson AP, Vincent JFV, Turner RM. The Mechanical Design of Nacre. Proc R Soc Ser B-Bio. 1988; 234:415–+. DOI: 10.1098/rspb.1988.0056
4. Chen AY, Zhong C, Lu TK. Engineering living functional materials. ACS Synth Biol. 2015; 4:8–11. DOI: 10.1021/sb500113b [PubMed: 25592034]
5. Purnick PE, Weiss R. The second wave of synthetic biology: from modules to systems. Nat Rev Mol Cell Biol. 2009; 10:410–422. DOI: 10.1038/nrm2698 [PubMed: 19461664]
6. Khalil AS, Collins JJ. Synthetic biology: applications come of age. Nat Rev Genet. 2010; 11:367–379. DOI: 10.1038/nrg2775 [PubMed: 20395970]
7. Ringler P, Schulz GE. Self-assembly of proteins into designed networks. Science. 2003; 302:106–109. DOI: 10.1126/science.1088074 [PubMed: 14526081]
8. Zhong C, et al. Strong underwater adhesives made by self-assembling multi-protein nanofibres. Nature nanotechnology. 2012; 9:858–866.
9. Ryadnov MG, Woolfson DN. Engineering the morphology of a self-assembling protein fibre. Nat Mater. 2003; 2:329–332. DOI: 10.1038/nmat885 [PubMed: 12704382]
10. Lee YJ, et al. Fabricating genetically engineered high-power lithium-ion batteries using multiple virus genes. Science. 2009; 324:1051–1055. DOI: 10.1126/science.1171541 [PubMed: 19342549]
11. Aggeli A, et al. pH as a trigger of peptide beta-sheet self-assembly and reversible switching between nematic and isotropic phases. J Am Chem Soc. 2003; 125:9619–9628. DOI: 10.1021/ja021047i [PubMed: 12904028]
12. Fichman G, Gazit E. Self-assembly of short peptides to form hydrogels: design of building blocks, physical properties and technological applications. Acta Biomater. 2014; 10:1671–1682. DOI: 10.1016/j.actbio.2013.08.013 [PubMed: 23958781]
13. Yan H, Park SH, Finkelstein G, Reif JH, LaBean TH. DNA-templated self-assembly of protein arrays and highly conductive nanowires. Science. 2003; 301:1882–1884. DOI: 10.1126/science.1089389 [PubMed: 14512621]
14. Seeman NC, Belcher AM. Emulating biology: Building nanostructures from the bottom up. p Natl Acad Sci USA. 2002; 99:6451–6455. DOI: 10.1073/pnas.221458298
15. Seeman NC. Nanomaterials based on DNA. Annu Rev Biochem. 2010; 79:65–87. DOI: 10.1146/annurev-biochem-060308-102244 [PubMed: 20222824]
16. Elbaz J, Yin P, Voigt CA. Genetic encoding of DNA nanostructures and their self-assembly in living bacteria. Nat Commun. 2016; 7:11179. [PubMed: 27091073]
17. Sleytr UB, Beveridge TJ. Bacterial S-layers. Trends Microbiol. 1999; 7:253–260. [PubMed: 10366863]
18. Feng YY, et al. Hybrid (Organic/Inorganic) Electrodes from Bacterially Precipitated CdS for PEC/Storage Applications. J Phys Chem C. 2017; 121:3734–3743. DOI: 10.1021/acs.jpcc.6b11387
19. Shenton W, Pum D, Sleytr UB, Mann S. Synthesis of cadmium sulphide superlattices using self-assembled bacterial S-layers. Nature. 1997; 389:585–587.
20. Marusak KE, et al. Cadmium sulphide quantum dots with tunable electronic properties by bacterial precipitation. Rsc Adv. 2016; 6:76158–76166. DOI: 10.1039/C6RA13835G [PubMed: 28435671]
21. Chen AY, et al. Synthesis and patterning of tunable multiscale materials with engineered cells. Nat Mater. 2014; 13:515–523. DOI: 10.1038/nmat3912 [PubMed: 24658114]
22. Payne S, et al. Temporal control of self-organized pattern formation without morphogen gradients in bacteria. Mol Syst Biol. 2013; 9:697. [PubMed: 24104480]
23. Tan C, Marguet P, You LC. Emergent bistability by a growth-modulating positive feedback circuit. Nat Chem Biol. 2009; 5:842–848. DOI: 10.1038/Nchembio.218 [PubMed: 19801994]

24. Stano NM, Patel SS. T7 lysozyme represses T7 RNA polymerase transcription by destabilizing the open complex during initiation. Journal of Biological Chemistry. 2004; 279:16136–16143. DOI: 10.1074/jbc.M400139200 [PubMed: 14764584]
25. Cao Y, et al. Collective Space-Sensing Coordinates Pattern Scaling in Engineered Bacteria. Cell. 2016; 165:620–630. DOI: 10.1016/j.cell.2016.03.006 [PubMed: 27104979]
26. Barnhart MM, Chapman MR. Curli biogenesis and function. Annu Rev Microbiol. 2006; 60:131–147. DOI: 10.1146/annurev.micro.60.080805.142106 [PubMed: 16704339]
27. Zhang RL, Xu YS, Wen BH, Sheng N, Fang HP. Enhanced Permeation of a Hydrophobic Fluid through Particles with Hydrophobic and Hydrophilic Patterned Surfaces. Scientific Reports. 2014; 4 doi: Artn 5738.
28. Nagapudi K, et al. Viscoelastic and mechanical behavior of recombinant protein elastomers. Biomaterials. 2005; 26:4695–4706. DOI: 10.1016/j.biomaterials.2004.11.027 [PubMed: 15763249]
29. Tuson HH, et al. Measuring the stiffness of bacterial cells from growth rates in hydrogels of tunable elasticity. Mol Microbiol. 2012; 84:874–891. DOI: 10.1111/j.1365-2958.2012.08063.x [PubMed: 22548341]
30. Basu S, Gerchman Y, Collins CH, Arnold FH, Weiss R. A synthetic multicellular system for programmed pattern formation. Nature. 2005; 434:1130–1134. DOI: 10.1038/nature03461 [PubMed: 15858574]
31. Liu C, et al. Sequential establishment of stripe patterns in an expanding cell population. Science. 2011; 334:238–241. DOI: 10.1126/science.1209042 [PubMed: 21998392]
32. Tabor JJ, et al. A synthetic genetic edge detection program. Cell. 2009; 137:1272–1281. DOI: 10.1016/j.cell.2009.04.048 [PubMed: 19563759]
33. Schaerli Y, et al. A unified design space of synthetic stripe-forming networks. Nat Commun. 2014; 5:4905. [PubMed: 25247316]
34. Song H, Payne S, Gray M, You L. Spatiotemporal modulation of biodiversity in a synthetic chemical-mediated ecosystem. Nat Chem Biol. 2009; 5:929–935. DOI: 10.1038/nchembio.244 [PubMed: 19915540]
35. Moon TS, Lou C, Tamsir A, Stanton BC, Voigt CA. Genetic programs constructed from layered logic gates in single cells. Nature. 2012; 491:249–253. DOI: 10.1038/nature11516 [PubMed: 23041931]
36. Fernandez-Rodriguez J, Yang L, Gorochowski TE, Gordon DB, Voigt CA. Memory and Combinatorial Logic Based on DNA Inversions: Dynamics and Evolutionary Stability. ACS Synth Biol. 2015; 4:1361–1372. DOI: 10.1021/acssynbio.5b00170 [PubMed: 26548807]
37. Andrianantoandro E, Basu S, Karig DK, Weiss R. Synthetic biology: new engineering rules for an emerging discipline. Mol Syst Biol. 2006; 2(2006):0028. [PubMed: 16738572]
38. Siuti P, Yazbek J, Lu TK. Synthetic circuits integrating logic and memory in living cells. Nat Biotechnol. 2013; 31:448–452. DOI: 10.1038/nbt.2510 [PubMed: 23396014]
39. Tamsir A, Tabor JJ, Voigt CA. Robust multicellular computing using genetically encoded NOR gates and chemical 'wires'. Nature. 2011; 469:212–215. DOI: 10.1038/nature09565 [PubMed: 21150903]
40. Rosenfeld N, Young JW, Alon U, Swain PS, Elowitz MB. Gene regulation at the single-cell level. Science. 2005; 307:1962–1965. DOI: 10.1126/science.1106914 [PubMed: 15790856]
41. Bennett MR, Hasty J. Microfluidic devices for measuring gene network dynamics in single cells. Nat Rev Genet. 2009; 10:628–638. DOI: 10.1038/nrg2625 [PubMed: 19668248]
42. Din MO, et al. Synchronized cycles of bacterial lysis for in vivo delivery. Nature. 2016; 536:81–85. DOI: 10.1038/nature18930 [PubMed: 27437587]
43. Balagadde FK, et al. A synthetic Escherichia coli predator-prey ecosystem. Mol Syst Biol. 2008; 4:187. [PubMed: 18414488]
44. Chen Y, Kim JK, Hirning AJ, Josic K, Bennett MR. SYNTHETIC BIOLOGY. Emergent genetic oscillations in a synthetic microbial consortium. Science. 2015; 349:986–989. DOI: 10.1126/science.aaa3794 [PubMed: 26315440]
45. Lander AD. Pattern, growth, and control. Cell. 2011; 144:955–969. DOI: 10.1016/j.cell.2011.03.009 [PubMed: 21414486]

46. Nguyen PQ, Botyanszki Z, Tay PK, Joshi NS. Programmable biofilm-based materials from engineered curli nanofibres. Nat Commun. 2014; 5:4945. [PubMed: 25229329]
47. Li Y, et al. Surface plasmon coupling enhanced dielectric environment sensitivity in a quasi-three-dimensional metallic nanohole array. Opt Express. 2010; 18:3546–3555. DOI: 10.1364/OE.18.003546 [PubMed: 20389363]
48. Grandidier J, Callahan DM, Munday JN, Atwater HA. Light Absorption Enhancement in Thin-Film Solar Cells Using Whispering Gallery Modes in Dielectric Nanospheres. Advanced Materials. 2011; 23:1272–+. DOI: 10.1002/adma.201004393 [PubMed: 21381129]
49. Han GQ, et al. Controllable synthesis of three dimensional electrodeposited Co-P nanosphere arrays as efficient electrocatalysts for overall water splitting. Rsc Adv. 2016; 6:52761–52771. DOI: 10.1039/c6ra04478f
50. Sun F, Zhang WB, Mahdavi A, Arnold FH, Tirrell DA. Synthesis of bioactive protein hydrogels by genetically encoded SpyTag-SpyCatcher chemistry. Proc Natl Acad Sci U S A. 2014; 111:11269–11274. DOI: 10.1073/pnas.1401291111 [PubMed: 25049400]
51. Chen L, et al. Two-dimensionality of yeast colony expansion accompanied by pattern formation. PLoS Comput Biol. 2014; 10:e1003979. [PubMed: 25504059]
52. Vallet-Regi M, Colilla M, Gonzalez B. Medical applications of organic-inorganic hybrid materials within the field of silica-based bioceramics. Chem Soc Rev. 2011; 40:596–607. DOI: 10.1039/c0cs00025f [PubMed: 21049136]
53. Hirst AR, Escuder B, Miravet JF, Smith DK. High-tech applications of self-assembling supramolecular nanostructured gel-phase materials: from regenerative medicine to electronic devices. Angew Chem Int Ed Engl. 2008; 47:8002–8018. DOI: 10.1002/anie.200800022 [PubMed: 18825737]
54. Goldberg M, Langer R, Jia X. Nanostructured materials for applications in drug delivery and tissue engineering. J Biomater Sci Polym Ed. 2007; 18:241–268. [PubMed: 17471764]
55. Langer R, Tirrell DA. Designing materials for biology and medicine. Nature. 2004; 428:487–492. DOI: 10.1038/nature02388 [PubMed: 15057821]
56. Niu Z, Liu L, Zhang L, Chen X. Porous graphene materials for water remediation. Small. 2014; 10:3434–3441. DOI: 10.1002/smll.201400128 [PubMed: 24619776]
57. Li H, Liu LF, Yang FL. Covalent assembly of 3D graphene/polypyrrole foams for oil spill cleanup. J Mater Chem A. 2013; 1:3446–3453. DOI: 10.1039/c3ta00166k
58. Newman SA, Frisch HL. Dynamics of skeletal pattern formation in developing chick limb. Science. 1979; 205:662–668. [PubMed: 462174]
59. Jernvall J, Thesleff I. Reiterative signaling and patterning during mammalian tooth morphogenesis. Mech Dev. 2000; 92:19–29. [PubMed: 10704885]
60. Kavanagh KD, Evans AR, Jernvall J. Predicting evolutionary patterns of mammalian teeth from development. Nature. 2007; 449:427–432. DOI: 10.1038/nature06153 [PubMed: 17898761]
61. Davies DG, et al. The involvement of cell-to-cell signals in the development of a bacterial biofilm. Science. 1998; 280:295–298. [PubMed: 9535661]
62. Asally M, et al. Localized cell death focuses mechanical forces during 3D patterning in a biofilm. Proc Natl Acad Sci U S A. 2012; 109:18891–18896. DOI: 10.1073/pnas.1212429109 [PubMed: 23012477]
63. Sambrook, J., Russell, DW. Molecular cloning : a laboratory manual. 3rd. Cold Spring Harbor Laboratory Press; 2001.
64. Cohen DJ, Morfino RC, Maharbiz MMA. Modified Consumer Inkjet for Spatiotemporal Control of Gene Expression. Plos One. 2009; 4 doi: Artn E7086.
65. Braunovic, M., Konchits, VV., Myshkin, NK. Electrical contacts : fundamentals, applications and technology. CRC Press; 2007.
66. Li LQ, Song WP, Zhang GY, Jia D. An electrical contact resistance model including roughness effect for a rough MEMS switch. J Micromech Microeng. 2012; 22 doi: Artn 115023.
67. Vogler M, Sheppard S. Electrical Contact Resistance under High Loads and Elevated-Temperatures. Weld J. 1993; 72:S231–S238.

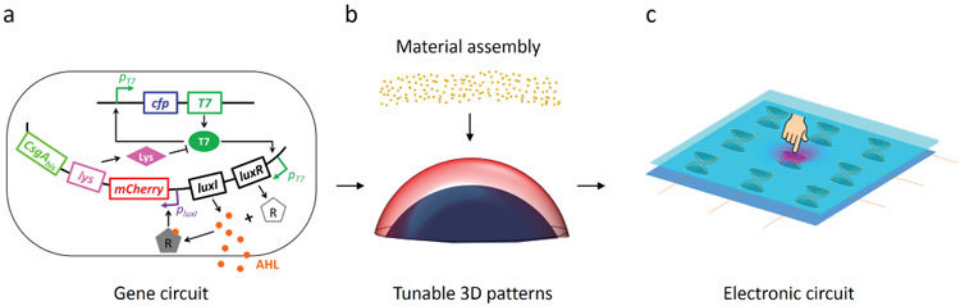

Figure 1. Programmable material fabrication using engineered pattern-forming bacteria

(a) The circuit consists of T7RNAP that activates its own expression as well as the expression of LuxR and LuxI. LuxI mediates synthesis of AHL, which drives expression of T7 Lysozyme, CsgA containing a 6×-His tag, and an mCherry reporter through activation of LuxR. The circuit is turned ON by exogenous addition of IPTG[22]. (b) Bacteria containing the curli-pattern circuit can form self-organized curli patterns in each colony, which can serve as the scaffold to assemble inorganic materials. (c) The schematic illustrates a “touch pad” that can sense and transduce local pressure variations. The dome shape represents the micro-structured material made from the colony; the orange lines represent conductive wires; and the two blue planes represent supporting surfaces.

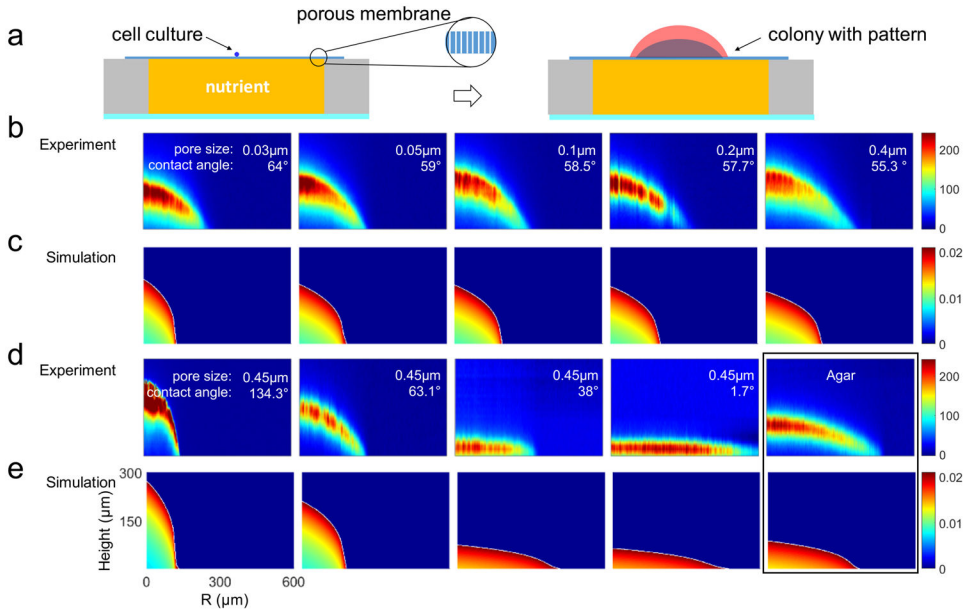

Figure 2. Bacterial growth and pattern formation on permeable membranes

(a) The bacterial colonies were grown on permeable membranes. We loaded 0.3% molten agarin 2×YT with IPTG and appropriate antibiotics in a Culture Well multiwell chambered coverslip (Grace Bio-Labs). After the agar solidified, we placed a permeable membrane on top of the culture well and printed bacteria onto the membrane surface. The diagram is not to scale. (b) Experimentally generated dome structures on membranes with different pore sizes. Each column represents the heat map of mCherry fluorescence patterns measured by a confocal microscope after 32 hrs incubation in both vertical (y-axis) and radial (x-axis) directions. The pore size varied from 0.03 to 0.4 μm, as indicated. The contact angles of these membranes varied slightly (from left to right: 64.0°, 59.0°, 58.5°, 57.7°, 55.3°). (c) Simulated dome structures on membranes with varying pore sizes. In our model, we assume that the pore size affects the radius expansion rate v and the nutrient influx rate α_1 (Eqs. (2) and (3)), respectively. Each column represents the heat map of simulated mCherry fluorescence patterns for the varying pore sizes. (d) Experimentally generated dome structures on membranes with different contact angles. Each column represents the heat map of mCherry fluorescence patterns measured by a confocal microscope after 32 hrs incubation in both vertical (y-axis) and radial (x-axis) directions. From left to right, the membrane is PVDF, PC, MCE, NC. The pore size of each membrane is 0.45 μm. Contact angle of each membrane is 134.3°, 63.1°, 38.0°, 1.7°. The most left image is colony directly grow on 0.3% 2×YT (PH=6.5) agar. (e) Simulated dome structures on membranes with different contact angles. In our model, we assume that the contact angle affects the radius expansion rate v according to Eq (2). Each column represents the heat map of mCherry fluorescence using a simulation with different v.

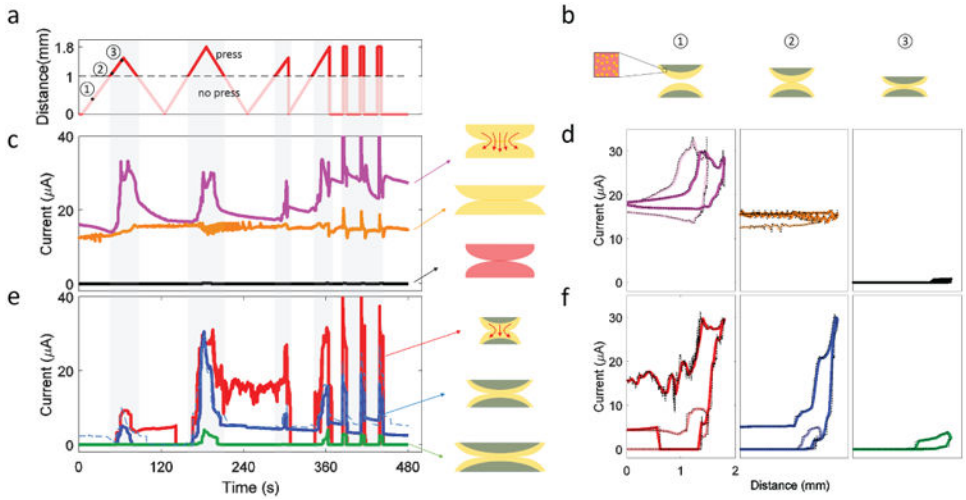

Figure 3. Patterned gold nanoparticles as a resettable pressure sensor

(a) Two opposing colonies were compressed with controlled distance. The distance indicates the displacement of the presser from its starting position. The presser starts to make contact with the device when the displacement is >1 mm. The gray areas in Fig. 3a, c, and e indicate the contact time between pressing device and colony sensor. (b) Different time points are labeled in Fig. 3a. The yellow-blue dome shape represents the colony; yellow dome represents the cells within the colony with gold assembly. The inset image is a higher magnification of the yellow section at nanoscale: gold nanoparticles bind on curli. At time point 3, upon making contact, the two colonies would experience increasing pressure with an increasing displacement distance. (c) Colonies with uniform gold nanoparticles exhibited no differential response to pressure. With uniform expression of induced curli in a colony, gold nanoparticles were uniformly assembled throughout the colony, as illustrated as the yellow solid spherical cap on the right-hand side. Magenta and orange lines indicate currents from colonies grown on membranes with pore sizes of 0.03 μm and 0.1 μm, respectively. The black line indicates response of colonies of pattern-forming bacteria grown on membrane with a pore size of 0.03 μm, without assembling gold nanoparticles (illustrated as the red spherical cap on the right-hand side). The red arrows indicate the electric current pathway. (d) Intensity of electric current as a function of the pressing distance for colonies not containing dome structured gold nanoparticles. The left panel shows responses from a pair of colonies grown on a membrane with a pore size of 0.03 μm. The light magenta line indicates a varying pressing distance from 0 to 1.5 mm; the magenta line indicates a varying pressing distance from 0 to 1.8 mm. The middle panel shows responses from a pair of colonies grown on a membrane with a pore size of 0.1 μm. The light orange line indicates a varying pressing distance from 0 to 1.5 mm; the orange line indicates a varying pressing distance from 0 to 1.8 mm. The right panel shows responses of a pair colonies of pattern-forming bacteria grown on a membrane with a pore size of 0.1 μm, without assembling the gold nanoparticles. The gray line indicates a varying pressing distance from 0 to 1.5 mm; the black line indicates a varying pressing distance from 0 to 1.8 mm. (e) Colonies with the dome structure exhibited differential pressure responses. The red, blue and green solid lines indicate responses from colonies grown on membranes with pore sizes of 0.05 μm, 0.2 μm, and 0.4 μm respectively. The dashed blue line indicates replicate experiment of the solid

blue line by using different electrochemical machine of the same model on a different day. The right-hand side illustrates colonies containing dome-structured gold nanoparticles. The red arrows indicate the electrons travel pathway. (f) Intensity of electric current as a function of the pressing distance for colonies containing dome structured gold nanoparticles. The left panel shows responses from a pair of colonies grown on a membrane with a pore size of 0.05 μm. The light red line indicates a varying pressing distance from 0 to 1.5 mm; the red line indicates a varying pressing distance from 0 to 1.8 mm. The middle panel shows responses from a pair of colonies grown on a membrane with a pore size of 0.2 μm. The light blue line indicates a varying pressing distance from 0 to 1.5 mm; the blue line indicates a varying pressing distance from 0 to 1.8 mm. The right panel shows responses of a pair colonies of pattern-forming bacteria grown on a membrane with a pore size of 0.4 μm. The green line indicates a varying pressing distance from 0 to 1.8 mm. Because there is no signal from the colony when the pressing distance is from 0- 1.5 mm, there is no light green line.

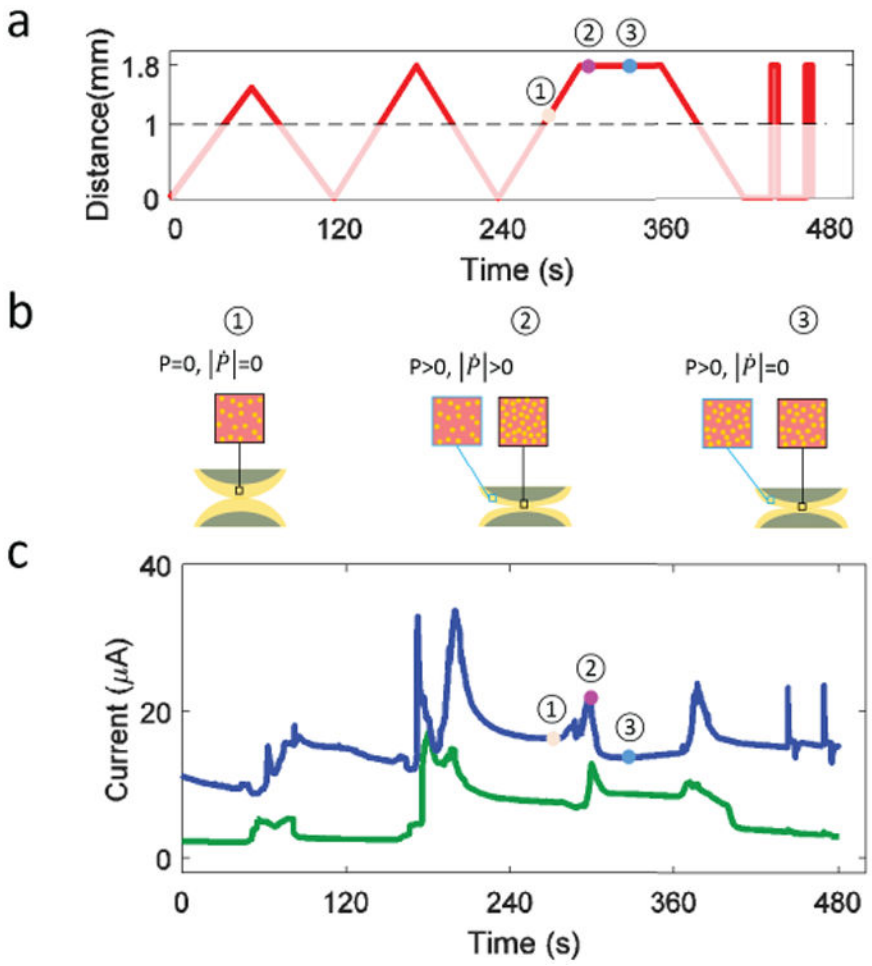

Figure 4. Patterned gold nanoparticles respond to pressure derivatives

(a) The pressing distance as a function of time, with the same device configuration as in Fig. 3a. (b) Distributions of gold nanoparticles corresponding to different pressure inputs. 1) the pressure is zero; 2) the pressure and its derivative are both positive; 3) the pressure is positive, but its derivative is zero. The three time points are labeled in Fig. 4A. (c) The pressure sensor responded strongly to changing pressure. The blue and green solid lines indicate current responses from colonies grown on membranes with pore sizes of 0.2 μm and 0.4 μm, respectively.

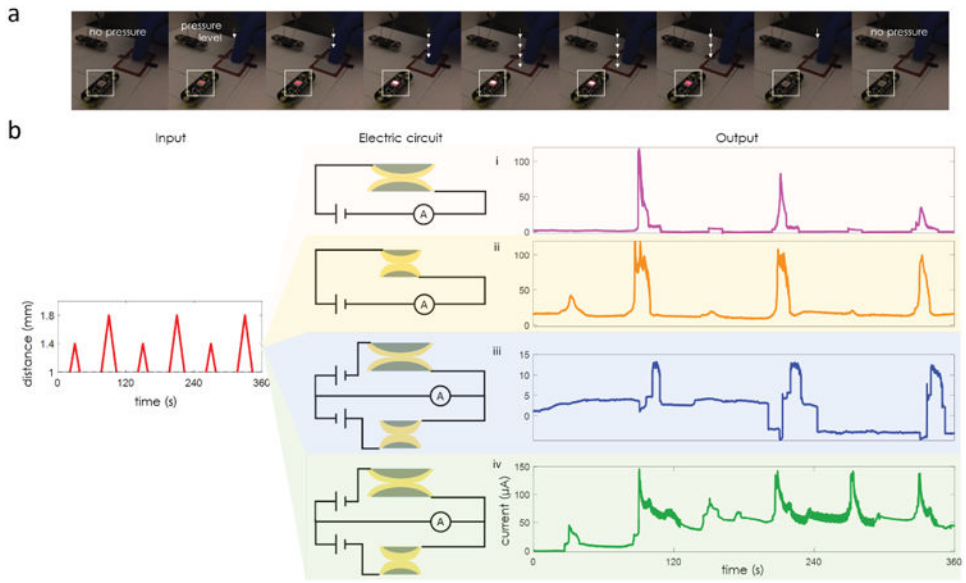

Figure 5. Robust signal processing by the bacterial pressure sensors

(a) Control of an LED light using a bacterial pressure sensor in response to manual operation. The images indicate LED light intensities when the sensor was pressed to varying degrees or released (also see Supplementary Video 1). All electronic components were from Electroninks Inc. (b) Construction of a noise filter and a signal amplifier using bacterially assembled gold domes. As in Fig. 3E, the input is the pressing distance as a function of time. Two sets of colonies were grown on the membranes with pore size of 0.2 μm and 0.05 μm, respectively. Panel i use the sets of small domes; panel ii use the sets of large domes; panels iii and iv are used the combination of the small and large sets of domes, but with different circuit design. Right of panel i and ii: the electric current readouts of these two sets of colonies being pressed separately. However, after combining the same sets of colonies with more complicated designs of the electronic circuits (panels iii and iv), substantial changes in the current signal were observed. Right panel iii: because the applied voltage polarities were opposite, the current signals from two sets of colonies canceled out. Only the current with higher amplitude was selected, therefore, the electronic circuit combined with the colonies functioned as a noise filter. Right panel iv: because the applied voltage polarities were the same, current signals from two sets of colonies summed up. Hence, the output was amplified in the form of the original input signal, and the electronic circuit functioned as a signal amplifier. The x-axes are of the same scale among i-iv panels. The units of y-axes are all in μA. To obtain reproducible results, all voltage providers used in the electronic circuits are of the same model (Keithley Series 6400 Picoammeters). The vertical alignment between the bottom of the presser and the center of the colony was carefully adjusted manually. The two pressers were controlled with the same mechanical pump to synchronize their operation.